Membrane filtration with complex branching pore morphology

Pejman Sanaei*
Courant Institute of Mathematical Sciences, New York University, New York, New York 10012-1110, USA

Linda J. Cummings
Department of Mathematical Sciences and Center for Applied Mathematics and Statistics, New Jersey Institute of Technology, Newark, New Jersey 07102-1982, USA

(Received 16 February 2018; published 21 September 2018)

Membrane filters are in widespread industrial use, and mathematical models to predict their efficacy are potentially very useful, as such models can suggest design modifications to improve filter performance and lifetime. Many models have been proposed to describe particle capture by membrane filters and the associated fluid dynamics, but most such models are based on a very simple structure in which the pores of the membrane are assumed to be simple circularly cylindrical tubes spanning the depth of the membrane. Real membranes used in applications usually have much more complex geometry, with interconnected pores that may branch and bifurcate. Pores are also typically larger on the upstream side of the membrane than on the downstream side. We present an idealized mathematical model, in which a membrane consists of a series of bifurcating pores, which decrease in size as the membrane is traversed. Feed solution is forced through the membrane by applied pressure and particles are removed from the feed by adsorption within pores (which shrinks them). Thus, the membrane's permeability decreases as the filtration progresses. We discuss how filtration efficiency depends on the characteristics of the idealized branching structure.

DOI: 10.1103/PhysRevFluids.3.094305

I. INTRODUCTION

Membrane filters are microporous films with specific pore size ratings for separating contaminants of any given size from a fluid. They are used in many industrial engineering processes. One of the most important and widespread applications is water purification [1], in which suspended particles, colloids, and macromolecules are removed from water using microfiltration and/or ultrafiltration. Membrane filters also service the biotech industry in many ways [2–5]; for example, they are used in artificial kidneys to remove toxic substances by hemodialysis and as an artificial lung to provide a bubble-free supply of oxygen in the blood [6]. Further applications include treatment of radioactive sludge [7], the cleaning of air or other gases [8], the production of osmotic power [9], and beer clarification [10], among many others.

There are two commonly used modes of filtration, each with advantages and disadvantages: (i) crossflow or tangential filtration and (ii) dead-end filtration. In the former case the feed flow is primarily parallel (tangential) to the surface of the membrane, while in the latter flow is perpendicular to the membrane surface. Membrane fouling inevitably occurs during filtration as the removed impurities deposit on or within the membrane but the extent and distribution of the fouling depends on the filtration mode and the membrane structure. In tangential-flow filtration, less

*ps168@nyu.edu

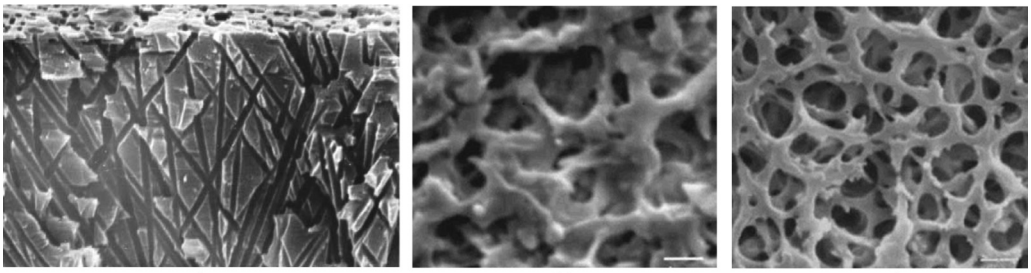

(a) (b) (c)

FIG. 1. Magnified membranes with various pore distributions and sizes from (a) Ref. [13] and (b) and (c) Ref. [4]. Photographs in (b) and (c) show samples of width 10 μm.

superficial membrane fouling is observed, due to the sweeping effect of the high-shear tangential flow on the membrane surface, while in dead-end filtration more extensive superficial membrane fouling occurs, but a higher flux can be achieved. We will focus on dead-end filtration in this paper. Membrane fouling may arise due to a combination of mechanisms: (i) adsorption, in which smaller particles are deposited within the membrane pores; (ii) blocking, in which particles larger than the pore size are sieved out and deposited at the pore entrance; and finally, (iii) once pores are blocked in this way, larger particles can form a cake on top of the membrane, adding additional resistance via a secondary porous layer on top. Using primarily empirical fouling laws, numerous investigations have been carried out of all three mechanisms (see, for example, [2,7,10–12], among many others).

In addition to empirical laws, a range of first-principles models has been proposed to describe particle capture by membrane filters and the associated fluid dynamics, but most such models are based on a very simple structure in which the pores of the membrane are assumed to be simple tubes spanning the depth of the membrane. Real membranes used in applications can have rather varied internal structure (see, e.g., Fig. 1), with interconnected pores that may branch and bifurcate, and pore-size variation across the membrane. Pores are typically larger on the upstream side of the membrane than on the downstream side, giving a porosity gradient in the depth of the membrane. It has long been known that porosity gradients affect filter performance in terms of both the filter lifetime and the total filtrate collected over the lifetime (as well as particle retention by the membrane), with negative porosity gradients (in the direction of flow) giving superior performance. This is intuitively obvious when considering the adsorptive fouling mechanism: Fouling begins at the upstream side of the membrane, hence those pores shrink fastest and so should be largest to maximize pore closure time.

Quantification of the effects of the membrane's internal morphology (the pores' shape, size, connectivity, and distribution within the membrane) on the filtration process, which is the main focus of this paper, has been considered by several authors, using a variety of modeling avenues (see, e.g., [14–27]). We highlight just a couple of the approaches most relevant to our work here. Dalwadi *et al.* [14] used homogenization theory to model the filter material as a collection of spherical obstructions, around which the feed solution must flow and whose size slowly varies across the membrane. This size variation models porosity gradients within the filter and the filter's performance can be investigated theoretically as a function of the porosity gradient. Griffiths *et al.* [16] made further contributions to quantitative understanding of the effects of pore-size depth variation, formulating a discrete network model that treats a membrane as a series of interconnected layers, each of which contains cylindrical channels (whose radius varies from one layer to the next) that may shrink under the action of adsorption or be blocked from above by deposition of a large particle. In our previous work [25], we considered perhaps the simplest continuum model of depth variation, in which the membrane consists of a series of identical axisymmetric pores spanning the entire membrane, with depth-dependent radius.

The goal of the present paper is to extend the scope of the work outlined above, deriving a general pore branching model that accounts for a range of membrane internal geometries and that allows for fouling by particle adsorption within pores. The paper is laid out as follows. In Sec. II we introduce a mathematical model for flow through a membrane with internal branching structure and propose the adsorptive fouling model. In Sec. III we introduce appropriate scalings and nondimensionalize the model. Sample simulations, which demonstrate the important effects of pore geometry and branching features, are presented in Sec. IV. We conclude in Sec. V with a discussion of our model and results in the context of real membrane filters and of future modeling directions. We also include two Appendixes: Appendix A, which sketches a model to account for fouling at the pore bifurcation junctions, and Appendix B, which outlines a simplified discrete model to describe the membrane fouling (which is much faster and cheaper to implement numerically, especially for asymmetric pore structures).

II. MATHEMATICAL MODELING

The modeling throughout this section assumes that the membrane is flat and lies in the (Y, Z) plane, with unidirectional incompressible Darcy flow, at superficial velocity $U(T)$, through the membrane in the positive X direction (that U does not depend on X is immediate from the unidirectionality and incompressibility). The membrane properties and flow are assumed homogeneous in the (Y, Z) plane, but membrane structure may vary internally in the X direction (depth-dependent permeability); thus we seek a solution in which properties vary only in X and in time T. Throughout this section we use uppercase letters to denote dimensional quantities; lowercase letters, introduced in Sec. III, will be dimensionless.

Two filtration forcing mechanisms are commonly used in applications: (i) constant pressure drop across the membrane specified and (ii) constant flux through the membrane specified. In the former case the flux will decrease in time as the membrane becomes fouled; in the latter, the pressure drop required to sustain the constant flux will rise as fouling occurs. We will focus on case (i) here and assume this in the following model description. With constant pressure drop P_0, the boundary conditions on the pressure $P(X, T)$ within the membrane are

$$P(0, T) = P_0, \quad P(D, T) = 0, \tag{1}$$

where D is the membrane thickness.

In this paper, we consider only one of the three fouling mechanisms described in the Introduction: fouling due to particle adsorption within the membrane pores (also known as standard blocking). Though pore blocking and cake formation are not difficult to incorporate in our model, including them here will make it harder to draw firm conclusions about the effects of pore geometry, particularly in the presence of some parametric uncertainty; hence we leave these effects for a future study. Furthermore, adsorptive fouling represents the most efficient (and therefore desirable) filtration in the sense that it is the only fouling mode that utilizes the membrane interior: It allows for filtration with pores that are much larger than the particles, so filtration can be achieved with minimal system resistance.

We consider a feed solution containing small particles (much smaller than the pore diameter), which are transported down pores and may be deposited on the internal pore walls. In the present work, we assume that all small particles behave identically; an extension of our study to consider multiple particle populations with different properties is left for future work. For such a feed solution our assumption of adsorptive fouling only should be a reasonable approximation. In our previous work [25], we modeled the filter membrane as a periodic lattice of identical axisymmetric pores, which traverse the membrane from the upstream to the downstream side, with radius varying in the depth of the membrane. In reality, and as noted in the Introduction, most membranes have a much more complex structure: Figure 1 shows just three examples of real filter membrane cross sections. Many membranes have depth structure that varies from large pores on the upstream side to much smaller pores on the downstream side, and large pores may branch into several smaller pores as the

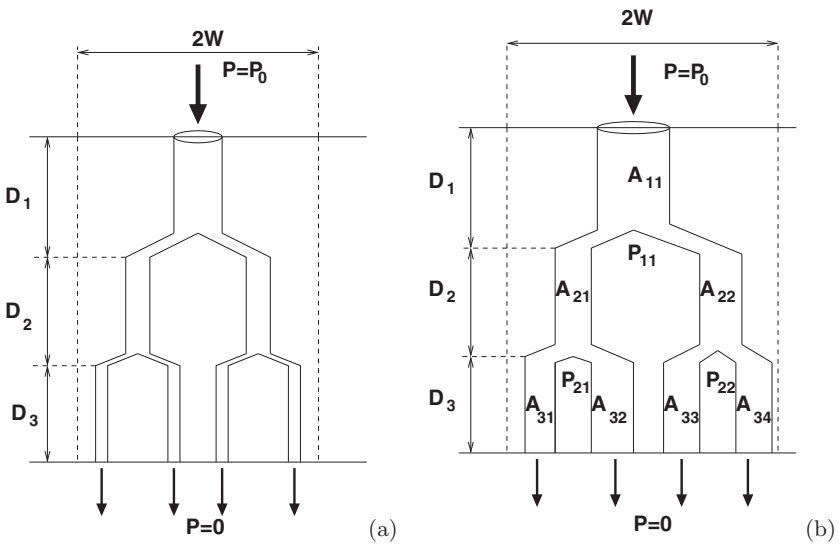

FIG. 2. Schematic of (a) symmetric and (b) asymmetric branching structures with three layers ($m = 3$), thicknesses D_1, D_2, and D_3, and specified pressure drop $P = P_0$. In (b) the radius of the jth pore in layer i and the pressure at the downstream end of this pore are A_{ij} and P_{ij}, respectively.

membrane is traversed. To begin to address this type of complexity, we will construct a simplified model in which a membrane consists of units that repeat periodically in the plane of the membrane in a square lattice pattern, with period $2W$. Within each lattice unit we assume that the membrane has a layered structure, exemplified by the sketch in Fig. 2(a): Here the period unit consists of a single circularly cylindrical pore on the upstream side which, after a distance D_1, bifurcates into smaller tubes (pores). Each of these then undergoes further bifurcation after distance D_2 and so on. This sequence of divisions generates a membrane with m layers, each layer containing twice as many pores as the previous layer. Clearly, many possible variants on this basic scenario could be imagined, including pores that recombine downstream: Our model will readily generalize to other cases. We will consider two scenarios in this paper: (i) a symmetric branching model in which the pores within each layer are identical and (ii) a more general asymmetric branching model [see Fig. 2(b)]. We will focus primarily on case (i) in this paper and outline the model in detail in Sec. II A below; our description for the asymmetric branching model requires minor modifications, described in Sec. II B.

A. Symmetric branching model

Here we consider all pores within a given membrane layer to be identical, initially circularly cylindrical, and perpendicular to the plane of the membrane. A simple case with three layers is schematized in Fig. 2(a): Each branching unit is assumed to stem from a single pore on the upstream surface. Layer i of the membrane occupies $X_{i-1} \leqslant X \leqslant X_i$, where $X_i = \sum_{j=0}^{i} D_j$, with $D_0 = 0$ defined for convenience. Assuming that the short pore-connection regions that are not perpendicular to the membrane have negligible resistance, this layered structure can be described using the Hagen-Poiseuille model: An individual pore in layer i of radius A_i has resistance $R_i = \int_{X_{i-1}}^{X_i} 8/\pi A_i^4 dX$ (even though pore radius does not vary in X initially, spatial variation will develop over time due to the fouling). Within a branching unit the ith layer contains ν_i pores and has depth D_i (for the case considered here, with only bifurcations of pores allowed, $\nu_i = 2^{i-1}$). Under these assumptions mass conservation shows that the cross-sectionally averaged pore velocity within each pore in

layer i, $\bar{U}_{\mathrm{p},i}(X)$, satisfies

$$\frac{\partial\left(\pi A_i^2 \bar{U}_{\mathrm{p},i}\right)}{\partial X} = 0, \quad X_{i-1} \leqslant X \leqslant X_i,\ 1 \leqslant i \leqslant m. \tag{2}$$

Note that the superficial Darcy velocity U through the membrane (independent of X as noted earlier) and averaged pore velocities for each layer are related by

$$(2W)^2 U = \pi \nu_i A_i^2 \bar{U}_{\mathrm{p},i}, \quad 1 \leqslant i \leqslant m, \tag{3}$$

by a simple flux balance argument. Within each layer U satisfies, approximately,

$$(2W)^2 U = -\frac{\nu_i}{\mu R_i}(P_i - P_{i-1}), \quad X_{i-1} \leqslant X \leqslant X_i,\ 1 \leqslant i \leqslant m, \tag{4}$$

where P_i $(1 \leqslant i \leqslant m-1)$ are the unknown interlayer pressures within the membrane (P_0 is the specified driving pressure and $P_m = 0$), providing m equations for U and the unknowns P_i. Solving successively for P_i we obtain

$$(2W)^2 U = \frac{P_0}{\mu R}, \tag{5}$$

where

$$R = \sum_{i=1}^{m} \frac{R_i}{\nu_i}, \quad R_i = \int_{X_{i-1}}^{X_i} \frac{8}{\pi A_i^4} dX. \tag{6}$$

Equation (6) captures the net resistance R of the microstructured membrane in terms of the resistances of its sublayers. For later use in comparing the performance of different pore structures, we define the so-called throughput, $V(T)$, which is the total volume of filtrate processed at time T and is commonly used experimentally to characterize membrane filter performance $V = \int_0^T (2W)^2 U dT$ or, equivalently,

$$\frac{\partial V}{\partial T} = (2W)^2 U, \quad V(0) = 0. \tag{7}$$

The model outlined above describes Darcy flow through a membrane with the specified microstructure. It must now be coupled to a fouling model that describes how the structure changes over time. Our fouling model is based on some of our earlier work [25], which used careful averaging of an advection-diffusion equation for the particle concentration over the pore cross section, in a distinguished Péclet number limit, to derive an equation for the axial advection of the small particles within the pores (assumed slender). A sink term represents the adsorption of particles at the pore wall as a flux into the wall, assumed driven by some radial force of attraction (likely of electrostatic origin in practice). We refer the reader to [25], Appendix A, for full details of our derivation; but briefly, assuming an asymptotic expansion for particle concentration C in powers of the pore aspect ratio squared, at leading order radial diffusion dominates the particle distribution within the pore, giving a particle concentration approximately uniform in the radial direction. The variation of concentration along the pore axis is determined by examining further terms (higher order) in the advection-diffusion equation. The direct analog of this model for pores in each sublayer of the membrane is

$$\bar{U}_{\mathrm{p},i} \frac{\partial C_i}{\partial X} = -\Lambda \frac{C_i}{A_i}, \quad X_{i-1} \leqslant X \leqslant X_i,\ 1 \leqslant i \leqslant m, \tag{8}$$

where C_i is the cross-sectionally averaged particle concentration in the pores of the ith layer, to be solved subject to specified particle concentration at the inlet,

$$C_1(0,T) = C_0, \tag{9}$$

and continuity of particle concentration from one layer to the next. The (dimensional) constant Λ models the physics of the attraction between particles and pore wall that is causing the deposition. The pore radius in each layer shrinks in response to the deposition according to

$$\frac{\partial}{\partial T}\left(\pi A_i^2\right) = -\Lambda\alpha(2\pi A_i)C_i \Rightarrow \frac{\partial A_i}{\partial T} = -\Lambda\alpha C_i, \quad X_{i-1} \leqslant X \leqslant X_i,\ 1 \leqslant i \leqslant m, \tag{10}$$

for some constant α (the pore shrinkage parameter, on the order of the particle volume), which simply assumes that the pore cross-sectional volume per unit depth shrinks at a rate given by the total volume of particles deposited locally. The initial pore radii are specified throughout the membrane

$$A_i(X, 0) = A_{i_0}, \quad X_{i-1} \leqslant X \leqslant X_i,\ 1 \leqslant i \leqslant m, \tag{11}$$

where A_{i_0} is the (constant, specified) initial radius of the pores in the ith layer.

As noted previously, this model describes the case of fouling by standard blocking (particle adsorption) only. Inclusion of other fouling modes such as pore blocking and cake formation is discussed briefly in Sec. V. In addition, we present and briefly discuss a simple model for fouling at pore junctions in Appendix A. Since trial simulations indicate that inclusion of such effects leads to only negligible changes to our results, we do not include junction fouling in the simulations and results of this paper.

B. Asymmetric branching model

The model above has the simplifying feature that all pores in a given layer are identical initially and thus, given the deterministic nature of our fouling model, remain so at later times. Real membranes do not possess such symmetry; hence we also formulate a more realistic model in which pores in the same layer are nonidentical. The same basic m-layered structure is assumed, however, in which a single pore at the upstream surface bifurcates into two smaller (nonidentical) tubes after distance D_1 and so on, again with $\nu_i = 2^{i-1}$ pores in layer i. These pores in general all have different radii, which we denote by A_{ij}, $1 \leqslant j \leqslant 2^{i-1}$ (the radius of the jth pore in layer i). The pressures at either end of this pore will be P_{ij} at the downstream end and $P_{i-1,[(j+1)/2]}$ at the upstream end[1] [see Fig. 2(b) for a simple schematic in the case of three layers]. In the first layer $i = 1$, there is just one pore of radius A_{11}, with upstream pressure $P_{01} = P_0$ specified. Here $\bar{U}_{\mathrm{p},ij}$ represents the cross-sectionally averaged velocity of the fluid in the jth pore in layer i and satisfies, approximately,

$$\pi A_{ij}^2 \bar{U}_{\mathrm{p},ij} = -\frac{1}{\mu R_{ij}}(P_{ij} - P_{i-1,[(j+1)/2]}), \quad 1 \leqslant i \leqslant m,\ 1 \leqslant j \leqslant 2^{i-1}, \tag{12}$$

where

$$R_{ij} = \int_{X_{i-1}}^{X_i} \frac{8}{\pi A_{ij}^4} dX \tag{13}$$

is the resistance of the jth pore in layer i. By a simple flux balance argument, the following relations hold between the superficial Darcy velocity U across the membrane and the pore velocities in each layer:

$$\begin{aligned} (2W)^2 U &= \pi A_{11}^2 \bar{U}_{\mathrm{p},11}, \\ \pi A_{ij}^2 \bar{U}_{\mathrm{p},ij} &= \pi A_{i+1,2j-1}^2 \bar{U}_{\mathrm{p},i+1,2j-1} + \pi A_{i+1,2j}^2 \bar{U}_{\mathrm{p},i+1,2j}, \quad 1 \leqslant i \leqslant m-1,\ 1 \leqslant j \leqslant 2^{i-1}. \end{aligned} \tag{14}$$

If the pore radii are specified then Eqs. (12) and (14) represent $2^m + 2^{m-1} - 1$ equations with $2^m + 2^{m-1} - 1$ unknowns, consisting of U, $\bar{U}_{\mathrm{p},ij}$ ($1 \leqslant i \leqslant m$ and $1 \leqslant j \leqslant 2^{i-1}$), and P_{ij} ($1 \leqslant i \leqslant m-1$

[1]The floor function $[x]$ is the greatest integer less than or equal to x.

and $1 \leqslant j \leqslant 2^{i-1}$); hence they can be solved uniquely. Consistent with the adsorption fouling model proposed in (8)–(11), we now have [analogous to (8) and (10)]

$$\bar{U}_{\mathrm{p},ij}\frac{\partial C_{ij}}{\partial X} = -\Lambda\frac{C_{ij}}{A_{ij}}, \quad \frac{\partial A_{ij}}{\partial T} = -\Lambda\alpha C_{ij}, \quad X_{i-1} \leqslant X \leqslant X_i,\ 1 \leqslant i \leqslant m,\ 1 \leqslant j \leqslant 2^{i-1}, \tag{15}$$

where C_{ij} is the cross-sectionally averaged particle concentration in the jth pore in layer i. We solve the model (12)–(15) subject to $C_{11}(0,T) = C_0$, $P_{11}(0,T) = P_0$, and $P_{mj}(D,T) = 0$ for $1 \leqslant j \leqslant 2^{m-1}$, with $A_{ij}(X,0)$ for $X_{i-1} \leqslant X \leqslant X_i$, $1 \leqslant i \leqslant m$, and $1 \leqslant j \leqslant 2^{i-1}$ all specified.

III. SCALING AND NONDIMENSIONALIZATION

To reduce the number of independent parameters, we introduce appropriate scales with which to nondimensionalize each model.

A. Symmetric branching model

We nondimensionalize (1)–(11) using the scalings

$$P_i = P_0 p_i, \quad (X, X_i, D_i) = D(x, x_i, d_i), \quad C_i = C_0 c_i, \quad A_i = W a_i, \quad R_i = \frac{8D}{\pi W^4}\hat{r}_i,$$
$$(U, \bar{U}_{\mathrm{p},i}) = \frac{\pi W^2 P_0}{32\mu D}(\hat{u}, \hat{\bar{u}}_{\mathrm{p},i}), \quad T = \frac{W}{\Lambda\alpha C_0}t, \quad Q = \frac{\pi W^4 P_0}{8\mu D}q, \quad V = \frac{\pi W^5 P_0}{8\mu D\Lambda\alpha C_0}v, \tag{16}$$

where $D = \sum_{i=1}^{m} D_i$ is the membrane thickness. This gives the dimensionless model for $\hat{u}(t)$, $c_i(x,t)$, $\hat{\bar{u}}_{\mathrm{p},i}(x,t)$, $\hat{r}_i(t)$, $a_i(x,t)$, $q(t)$, and $v(t)$ (dimensionless Darcy velocity, averaged particle concentration, averaged pore velocity, pore resistance, pore radii in the ith layer, flux, and throughput, respectively),

$$\hat{u} = \frac{1}{\sum_{i=1}^{m}\hat{r}_i/\nu_i}, \quad \hat{u} = \nu_i\frac{\pi a_i^2}{4}\hat{\bar{u}}_{\mathrm{p},i}, \tag{17}$$

$$\hat{r}_i = \int_{x_{i-1}}^{x_i}\frac{dx}{a_i^4}, \tag{18}$$

$$\bar{u}_{\mathrm{p},i}\frac{\partial c_i}{\partial x} = -\hat{\lambda}\frac{c_i}{a_i}, \quad x_{i-1} \leqslant x \leqslant x_i, \quad \hat{\lambda} = \frac{32\Lambda\mu D^2}{\pi P_0 W^3}, \tag{19}$$

$$\frac{\partial a_i}{\partial t} = -c_i, \tag{20}$$

with boundary and initial conditions

$$c_1(0,t) = 1, \quad a_i(0) = a_{i_0}, \tag{21}$$

where $1 \leqslant i \leqslant m$, and $a_{i_0} \in (0,1)$ are specified.

Using Eq. (17), one can define a dimensionless membrane resistance $\hat{r}(t)$, consistent with (5), as

$$\hat{r}(t) = \sum_{i=1}^{m}\frac{\hat{r}_i}{\nu_i}. \tag{22}$$

Note that, while this definition is in a sense "natural," typically it leads to very large values for $\hat{r}$ and as a consequence very small values for $\hat{u} = 1/\hat{r}$, specifically for a membrane with many layers. Our initial choice for the scalings in (16) makes sense based on a single pore (see our previous work [25]) but is not appropriate for a system with multiple layers and branching. Hence, we make

a further rescaling based on a typical value $\hat{r}_0$ of the resistance as defined in (22).[2] Therefore, we define

$$(r, r_i) = \frac{1}{\hat{r}_0}(\hat{r}, \hat{r}_i), \quad (u, \bar{u}_{\mathrm{p},i}) = \hat{r}_0(\hat{u}, \hat{\bar{u}}_{\mathrm{p},i}), \quad \lambda = \hat{r}_0\hat{\lambda}, \quad 1 \leqslant i \leqslant m, \tag{23}$$

where r, r_i, u, $\bar{u}_{\mathrm{p},i}$, and λ are the new dimensionless resistance, pore resistance, Darcy velocity, averaged pore velocity, and particle-wall attraction coefficient, respectively. Using these new scalings, (17)–(19) and (22) give

$$u = \frac{1}{\sum_{i=1}^{m} r_i/\nu_i}, \quad u = \frac{\pi}{4}\nu_i a_i^2 \bar{u}_{\mathrm{p},i}, \tag{24}$$

$$r_i = \frac{1}{\hat{r}_0}\int_{x_{i-1}}^{x_i} \frac{dx}{a_i^4(x)}, \tag{25}$$

$$\bar{u}_{\mathrm{p},i}\frac{\partial c_i}{\partial x} = -\lambda\frac{c_i}{a_i}, \quad \lambda = \frac{32\Lambda\mu D^2\hat{r}_0}{\pi P_0 W^3}, \tag{26}$$

$$r(t) = \sum_{i=1}^{m} \frac{r_i}{\nu_i} \tag{27}$$

for $1 \leqslant i \leqslant m$, while (20) and (21) still hold. Recall that in the case of bifurcating pores, $\nu_i = 2^{i-1}$.

B. Asymmetric branching model

We nondimensionalize the model (12)–(15), using the same scalings as in (16) and (23), giving the dimensionless model for $u(t)$, $c_{ij}(x,t)$, $\bar{u}_{\mathrm{p},ij}(x,t)$, $r_{ij}(t)$, $p_{ij}(x,t)$, and $a_{ij}(x,t)$ (dimensionless Darcy velocity, averaged particle concentration, averaged pore velocity, pore resistance, interlayer pressures, and pore radii within the jth pore in layer i, respectively),

$$4u = \pi a_{11}^2 \bar{u}_{\mathrm{p},11}, \quad a_{ij}^2\bar{u}_{\mathrm{p},ij} = a_{i+1,2j-1}^2\bar{u}_{\mathrm{p},i+1,2j-1} + a_{i+1,2j}^2\bar{u}_{\mathrm{p},i+1,2j}, \tag{28}$$

$$\pi a_{ij}^2\bar{u}_{\mathrm{p},ij} = -\frac{4}{r_{ij}}(p_{ij} - p_{i-1,[(j+1)/2]}), \tag{29}$$

$$r_{ij} = \frac{1}{\hat{r}_0}\int_{x_{i-1}}^{x_i} \frac{dx}{a_{ij}^4(x)}, \tag{30}$$

$$\bar{u}_{\mathrm{p},ij}\frac{\partial c_{ij}}{\partial x} = -\lambda\frac{c_{ij}}{a_{ij}}, \quad \lambda = \frac{32\Lambda\mu D^2\hat{r}_0}{\pi P_0 W^3}, \tag{31}$$

$$\frac{\partial a_{ij}}{\partial t} = -c_{ij}, \tag{32}$$

where $1 \leqslant i \leqslant m$ and $1 \leqslant j \leqslant 2^{i-1}$. We solve the model (28)–(32) subject to boundary and initial conditions

$$\begin{aligned} c_{11}(0,t) = 1, \quad a_{ij}(0) = a_{ij_0} \quad \text{for } 1 \leqslant i \leqslant m,\ 1 \leqslant j \leqslant 2^{i-1} \\ p_{01}(t) = 1, \quad p_{mj} = 0 \quad \text{for } 1 \leqslant j \leqslant 2^{m-1}, \end{aligned} \tag{33}$$

where $0 < a_{ij_0} < 1$ are specified.

[2] In most cases we take $\hat{r}_0 = 15\,000$ to be the initial dimensionless resistance given by (22), since we will most often compare equal resistance systems (see Sec. IV).

IV. RESULTS

In this section, we present some simulations of the models (20), (21), (24)–(27) (symmetric case), and (28)–(33) (asymmetric case) described in Sec. III above. We use an implicit finite-difference method with 100 grid points per pore to solve the equations numerically and we pay particular attention to how results depend on the branch configuration, as specified by the initial conditions on the pore radii. Other than parameters related to the initial membrane geometry, our model contains one dimensionless parameter λ, which captures the physics of the attraction between particles and the pore wall. Its value is unknown and may vary widely between systems depending on the detailed structure of the filter membrane and on the nature of the feed solution. In the absence of firm data we take $\lambda = 30$ for most simulations and briefly investigate the effect of varying λ later in Fig. 5. Methods of determining this parameter (which depends on the characteristics of both feed and membrane) for a given experimental system are discussed in Sec. V.

A. Symmetric branching model results

1. Equal-thickness layers

We first consider the case in which all layers are equally spaced, with $d_i = 1/m$. For the simple bifurcating pore model, $\nu_i = 2^{i-1}$ for $1 \leqslant i \leqslant m$; therefore, (25) and (27) together give dimensionless membrane resistance as

$$r(t) = \frac{1}{\hat{r}_0} \sum_{i=1}^{m} \frac{1}{2^{i-1}} \int_{x_{i-1}}^{x_i} \frac{dx}{a_i(x,t)^4}. \tag{34}$$

In order to make a meaningful comparison, we run simulations for pore structures that have the same initial membrane resistance $r_0 = r(0)$. This means that we are comparing membranes that perform identically when no fouling occurs; they would yield identical (constant) flow rates for a given transmembrane pressure difference when filtering pure water.

Furthermore, in order to keep the number of variable parameters small, we assume that the initial pore radius decreases geometrically in the depth of the membrane; that is, we take $a_{i_0} = a_{1_0}\kappa^{i-1}$ to be the initial radius of the pores in the ith layer, where a_{1_0} is the initial radius of the pore in the first layer and κ is the geometric ratio. Therefore, by fixing the initial resistance r_0 [as defined by (34) with $t = 0$] and varying the geometric coefficient κ, we can investigate a range of membrane morphologies. Note that, with r_0 and κ specified, the radius of the pore in the top layer will be determined; in particular, as κ increases, the initial pore radius in the top layer must decrease and vice versa (in order to keep total membrane resistance fixed). More specifically, setting $t = 0$ in (34) and using $a_i(x,0) = a_{1_0}\kappa^{i-1}$ gives

$$a_{1_0} = \left(\frac{1}{m r_0 \hat{r}_0} \sum_{i=1}^{m} \frac{1}{\kappa^{4(i-1)} 2^{i-1}} \right)^{1/4}. \tag{35}$$

A selection of results is shown in Fig. 3: We simulate the model (20), (21), and (24)–(27) for five different values of the geometric coefficient ($\kappa = 0.6$, 0.65, 0.707, 0.75, and 0.8), with deposition parameter $\lambda = 30$, number of layers $m = 5$, and initial dimensionless membrane resistance $r_0 = 1$. Note that the chosen range of κ values includes cases where membrane porosity is increasing ($\kappa > 1/\sqrt{2}$), uniform ($\kappa = 1/\sqrt{2} \approx 0.707$), and decreasing ($\kappa < 1/\sqrt{2}$) in the direction of flow.

Figures 3(a) and 3(b) show the pore radii at the top (upstream side) of each layer, $a_i(x_i, t)$, versus time, for $\kappa = 0.6$ and 0.8, respectively (results for $\kappa = 0.65$, 0.707, 0.75 are suppressed here since the evolution is qualitatively very similar). A notable feature of these plots is that pore closure occurs first in the upstream membrane surface layer, at least for the model parameters considered here. This may be understood qualitatively as follows. When the (identical) pores in any layer are near closure, the fluid velocity everywhere within the membrane tends to zero. In regions of the membrane where c is not already small, this leads to large spatial gradients in c [see (19)], which

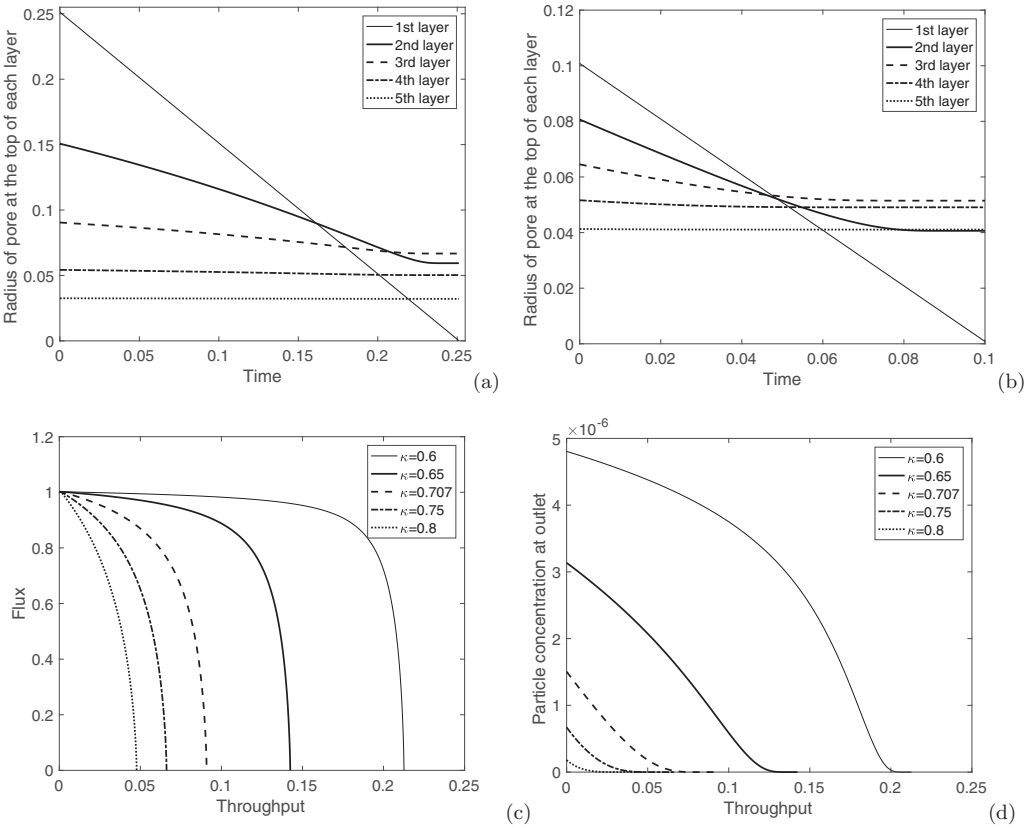

FIG. 3. Symmetric branching model. (a) and (b) Pore radius evolution at the top of each pore $a_i(x_i, t)$ for equal (initial) resistance membrane structures, where the initial pore radii in subsequent layers are geometrically decreasing, with geometric coefficient κ: (a) $\kappa = 0.6$ and (b) $\kappa = 0.8$. Also shown is the throughput $v(t)$ vs (c) total flux $q(t)$ and (d) particle concentration at outlet $c_m(1, t)$, for several different κ values shown in the legend. In all cases $r_0 = 1$, $\lambda = 30$, and the number of layers $m = 5$.

in turn leads to $c_{i-1}(x_{i-1}, t) \gg c_i(x_i, t)$ (again for i such that c_i is not already small; recall that $0 < c \leqslant 1$ is monotonically decreasing in x). It follows [Eq. (20)] that the closure rate of pores in downstream layers within the membrane drops relative to the rate in upstream layers, with the closure rate of the pore in the first layer dominating, eventually catching up with other pores, and closing first.

The closure time t_f, which is the time at which the membrane no longer permits flow and filtration ceases, varies with the geometric coefficient. For the scenarios shown in Fig. 3, our model predicts that the smaller the geometric coefficient, the larger the closure time; this appears to be primarily because, with initial total resistance fixed, the initial pore radius in the first layer is wider for a branching structure with a smaller geometric coefficient and (as discussed above) this is always the pore that closes first. Though we do not show the results for pore radii $a_i(t)$ in each layer versus time for the intermediate κ values $\kappa = 0.65, 0.707, 0.75$, those cases also bear out this prediction. Note that from Eqs. (20) and (21) it follows that $\frac{\partial a_1}{\partial t}|_{x=0} = -1$, hence (since this pore closes first) the closure time is exactly $t_f = a_{1_0}$.

Figure 3(c) shows flux-throughput graphs for the membrane structures with the chosen values of the geometric coefficients κ. The flux-throughput graph plots the instantaneous flux through the membrane at any given time versus the total volume of filtrate processed at that time (throughput) and is a common experimental characterization of membrane filter performance. Since the flux

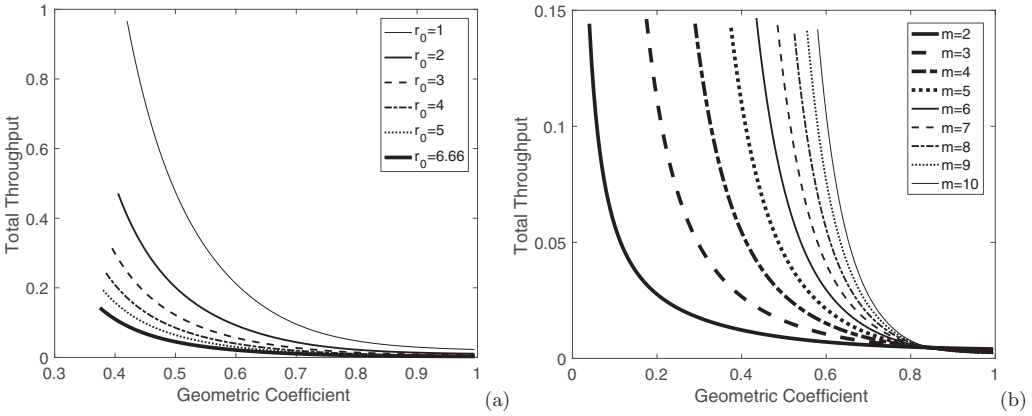

FIG. 4. Symmetric branching model: total throughput $v(t)$ versus geometric coefficient κ with $\lambda = 30$ for (a) several different values of dimensionless initial resistance r_0 with number of layers $m = 5$ and (b) several different numbers of layers m, with $r_0 = 6.66$.

is directly proportional to the superficial Darcy velocity and is depth independent, we define dimensionless flux for our model by $q(t) = u(0, t)$; dimensionless throughput is then given by $v(t) = \int_0^t q(t')dt'$ [see also (7)]. The graphs in Fig. 3(c) collectively demonstrate that, although all branch structures give the same initial average membrane resistance (manifested by the same initial flux), they exhibit significant differences in performance over time. In particular, if performance is characterized by total throughput over the filter lifetime then (for the chosen model parameters) branch structures with wider pores in the top layer (upstream side) give notably better performance overall, with more filtrate processed under the same conditions. The minimum total throughput is given by the branch structure with the narrowest pore on the upstream side ($\kappa = 0.8 > 1/\sqrt{2}$; here the porosity is increasing in the depth of the membrane), which exhibits rapid closure.

Another key consideration in evaluating membrane performance is the concentration of particles remaining in the filtrate as it exits the membrane, $c_m(1, t)$: In general, a lower particle concentration at the outflow side of the membrane indicates superior separation efficiency. Figure 3(d) plots $c_m(1, t)$ versus throughput for each of the chosen geometric coefficients. The results here are consistent with those of the flux–throughput graphs of Fig. 3(c); in particular, membranes with narrow pores in the first layer of the branching network (or with larger geometric coefficients κ) give poorer performance by this measure also, exhibiting inferior particle retention compared with membranes whose pores are wider on the upstream side. A noteworthy feature here is that in the "best-performing" case $\kappa = 0.6$, particle retention actually *worsens* during filtration initially, indicated by an increasing value of $c_m(1, t)$. This type of behavior may be observed in real membranes and has been predicted in discrete particle simulations of filtration pore networks (see, e.g., [28]), though not in continuum-based models such as ours. Though the effect is minor here, it is important to be aware that particle removal efficiency can be nonmonotonic and to predict conditions under which such behavior will occur, since a user needs to be able to rely on particle retention always meeting the desired tolerance.

Figures 4(a) and 4(b) further illustrate the model predictions, plotting throughput versus the geometric coefficient for several different scenarios. In Fig. 4(a) the number of layers is fixed, $m = 5$, and total throughput is plotted versus the geometric coefficient for several different values of the initial membrane resistance r_0. Note that for lower resistance membranes, where pores must be large (relative to the containing period box), the range of realizable geometric coefficients is bounded below. Needless to say, as initial membrane resistance increases, the performance of the filter (as measured by total throughput) decreases. Consistent with our results in Fig. 3, for fixed initial resistance a larger geometric coefficient always results in less total throughput.

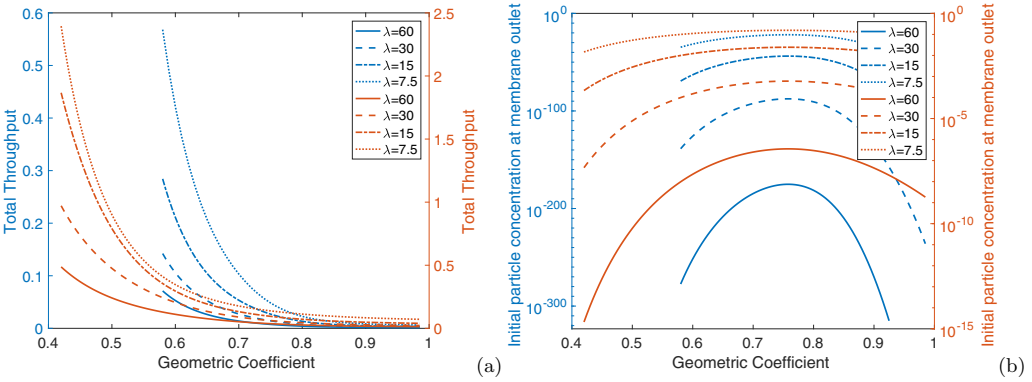

FIG. 5. Symmetric branching model: (a) total throughput $v(t)$ and (b) initial particle concentration at the pore outlet $c_m(1, 0)$, versus the geometric coefficient κ for several different values of λ, with $m = 5$ and $r_0 = 1$ (orange curves) and $m = 10$ and $r_0 = 6.66$ (black curves).

In Fig. 4(b), the dimensionless initial membrane resistance is fixed and throughput is again plotted as a function of geometric coefficient for several different values of m (the number of layers in the structure). Note that, with the assumed form of the branching geometry, a structure with more layers tends to have a higher resistance (for a given geometric coefficient κ, the numerous pores in the downstream layers become very small). Therefore, in order to access a wide range of geometric coefficients with a many-layered structure, we choose a sufficiently large value of the dimensionless initial resistance r_0 [see (34)] to illustrate the effect of changing the number of layers; here $r_0 = 6.66$. Our results indicate that for a fixed geometric coefficient and fixed initial resistance, better performance is observed for branching configurations with more layers. [Note that in order to fix both the geometric coefficient and the resistance while increasing the number of layers, as was done to calculate the points on each curve in Fig. 4(b) for each value on the horizontal axis, the size of the pore in layer 1 a_{1_0} must increase (see 35).] We also carried out simulations (results not shown here) to generate the equivalent results for throughput versus a_{1_0} (with r_0 held fixed) so that κ must change as the number of layers m is varied for each a_{1_0} value: We find that as m increases, the throughput again increases, but the effect is not as dramatic as in Fig. 4(b).

It is also of interest to study the influence of the dimensional deposition or "stickiness" coefficient Λ on results. This coefficient appears in our choice of timescale $T = W/\Lambda\alpha C_0 t$, as well as in the dimensionless parameter $\lambda = 32\Lambda\mu D^2\hat{r}_0/\pi P_0 W^3$ [see (16) and (26)]. When we change Λ, we therefore also rescale time in simulations.[3] Figure 5(a) illustrates the effect of changing λ, plotting throughput versus the geometric coefficient for several different values of the deposition coefficient λ. Two sets of simulations are shown: a five-layer membrane ($m = 5$) with initial dimensionless resistance $r_0 = 1$ (orange curves) and a ten-layer membrane ($m = 10$) with initial dimensionless resistance $r_0 = 6.66$ (black curves). Here again we find that, for all values of λ considered, the maximal total throughput is achieved at the smallest geometric coefficient (the highest permeability gradient); equivalently, at fixed initial resistance the optimum throughput is obtained for the branch configuration with pores as wide as possible in the first layer. In all cases, as λ increases, total throughput decreases, as anticipated (improved particle retention leads to faster clogging).

Figure 5(b) shows the initial particle concentration at the membrane outlet $c_m(1, 0)$ versus the geometric coefficient κ, for several different values of λ with $m = 5$ and $r_0 = 1$ (orange curves) and $m = 10$ and $r_0 = 6.66$ (black curves). These results indicate that for larger values of λ there is little variation in $c_m(1, 0)$, but at smaller values of λ the geometric coefficient κ can have a significant effect on the proportion of particles removed (note the logarithmic scale used on the

[3]Such rescaling of time does not, however, affect the flux-throughput graphs.

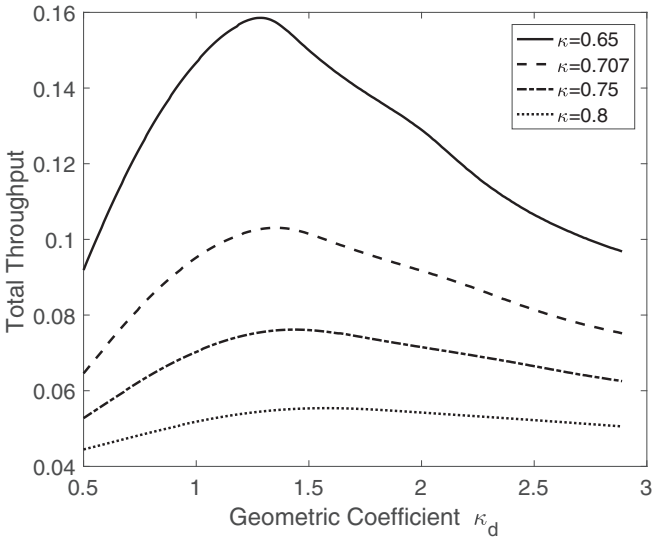

FIG. 6. Symmetric branching model: total throughput $v(t)$ versus membrane layer thickness geometric coefficient κ_d with $\lambda = 30$, $r_0 = 1$, $m = 5$ layers, and geometric coefficients $\kappa = 0.65, 0.707, 0.75, 0.8$.

vertical axis). An observation common to all the graphs in Fig. 5(b) is the existence of a local maximum in $c_m(1, 0)$ as κ is increased, located somewhere between 0.7 and 0.8. We note that the value $\kappa = 1/\sqrt{2} \approx 0.707$ corresponds to a membrane of uniform porosity in the depth of the filter, suggesting that filters with either decreasing *or* increasing porosity in the membrane depth are preferable to those of uniform porosity as regards particle removal (though not as regards total throughput). In all cases, as λ increases the initial outlet particle concentration decreases as expected.

2. Variable-thickness layers

The assumption of equal-thickness layers made in the preceding section is convenient, but likely not optimal. Hence here we briefly consider the effect of allowing layers of variable thickness. To keep the parameter space manageable, we again assume that the layer thickness variation satisfies a geometric progression $d_{i+1} = \kappa_d d_i$. We solve the model represented by Eqs. (20), (21), and (24)–(27) and investigate how results depend on κ_d. Results are summarized in Fig. 6 for the initial membrane resistance $r_0 = 1$ with the number of layers $m = 5$. Here the total throughput is plotted as a function of the layer thickness geometric coefficient κ_d for four different values of the pore-radius geometric coefficient κ. As already observed, throughput increases significantly as κ decreases (larger negative porosity gradients in the depth of the filter), but we now also see a strong dependence on κ_d. In particular, it is clear that the default value of $\kappa_d = 1$ considered previously is never optimal, and indeed, it is far from optimal for the preferred smaller values of κ. Interestingly, in the scenarios explored here, the optimal value of κ_d varies little with either r_0, m, or κ, taking values in the range (1.25,1.45) for all considered simulations. These results indicate that, for optimal results, subsequent layers should have pores of smaller radius ($\kappa < 1$), but greater length ($\kappa_d > 1$).

The existence of an optimal value for κ_d may be understood as follows. For a fixed initial resistance, increasing κ_d (i.e., making downstream pores longer) results in increasing a_{1_0}, which has been shown to increase total throughput. However, for fixed m, increasing κ_d also reduces the length of the first layer pore and at some point (once the first pore becomes sufficiently short) many particles will leak through into lower layers and pollute the downstream pores, which are much narrower and hence more sensitive to standard blocking. Thus, total throughput will ultimately decrease once κ_d increases beyond a certain value.

We observe also that the optimal value of κ_d described above was found to be an increasing function of λ (results not shown here). To see why this should be, consider an optimal scenario as explained above and then suppose we increase the value of λ so that particles are now more strongly attracted to the pore wall. Since particle removal now occurs on a shorter length scale along the pore axis, the first pore will still consume most of the particles even if it is very short; hence to obtain the optimal scenario we may shrink its length (and increase its radius), corresponding to a larger value of κ_d. Similarly, for smaller λ the optimum κ_d will be smaller. This prediction was explored numerically and found to hold for λ values between 0.001 and 1000.

B. Asymmetric branching model results: Equal-thickness layers

Since the symmetric branching geometry is highly idealized, we also briefly study asymmetric branching pore structures in a simple subcase: The same layered structure is assumed, but the pores in the second layer are nonidentical. Beyond the second layer the whole structure is supposed to divide into two subbranches, left (L) and right (R), with pores decreasing geometrically in the depth of the membrane with geometrical coefficients κ_L and κ_R, respectively. Consequently, the total dimensionless membrane resistance is given by

$$r(t) = r_1(t) + \left(\frac{1}{r_R(t)} + \frac{1}{r_L(t)}\right)^{-1}, \tag{36}$$

where $r_1(t)$, $r_R(t)$, and $r_L(t)$ are resistances of the first layer and the right and left subbranches, respectively, and can be obtained as

$$r_1(t) = \frac{1}{\hat{r}_0}\int_0^{x_1} \frac{dx}{a_1^4(x,t)}, \quad r_{R\,(L)}(t) = \frac{1}{\hat{r}_0}\sum_{i=2}^{m}\frac{1}{2^{i-2}}\int_{x_{i-1}}^{x_i}\frac{dx}{a^4_{R_i\,(L_i)}(x,t)}, \tag{37}$$

with

$$a_{Ri}(0) = a_{1_0}\kappa_R^{i-1}, \quad a_{Li}(0) = a_{1_0}\kappa_L^{i-1} \quad \text{for } 2 \leqslant i \leqslant m, \tag{38}$$

where a_1 is the radius of the pore in the first layer [with $a_1(0) = a_{1_0}$] and a_{Ri} and a_{Li} are the ith layer pore radii in the right and left subbranches, respectively. Equation (36) is analogous to Kirchhoff's circuit laws and can be easily obtained from our flow model [see (4)].

In Figs. 7(a) and 7(b), we present simulations where the ratio of right and left branch geometric coefficients is fixed as $\kappa_R/\kappa_L = 0.8$, while the initial radius of the inlet pore a_{1_0} was chosen to be the same as in the symmetric branching model results of Figs. 3(a) and 3(b). The dimensionless deposition coefficient is set to $\lambda = 30$, the number of layers is fixed at $m = 5$, and the initial dimensionless membrane resistance [defined in (36)] is $r(0) = r_0 = 1$ for direct comparison with Fig. 3. Similar to the symmetric branching model, pore closure occurs first in the top layer for all cases shown here. Hence, in all cases shown, the time to total blockage (the duration of the filtration process) is the same as for the symmetric branching structure.

Figure 7(c) illustrates the flux-throughput characteristics for this asymmetric case (red curves) and provides an explicit comparison to the corresponding symmetric case [black curves; where line styles match those of the red curves, the same initial values for the inlet pore radius are used; see the original results in Fig. 3(c)]. Note that in all cases shown, both symmetric and asymmetric, the initial net membrane resistance is the same: $r_0 = 1$. Our results here indicate that breaking symmetry reduces filtration efficiency: All asymmetric cases considered lead to less total throughput than the corresponding symmetric case. Figure 7(d) shows particle concentration at the outlet, $c_{mj}(1,t)$ for $j = 1, \ldots, 2^{m-1}$, versus instantaneous throughput for the left (black curves) and right (red curves) subbranches, for the above given parameters. Note that, due to the symmetry of each subbranch, the particle concentration at outlet in all pores of the left subbranch will be the same, as will that for all pores in the right subbranch; hence for each simulation we see just two distinct concentration

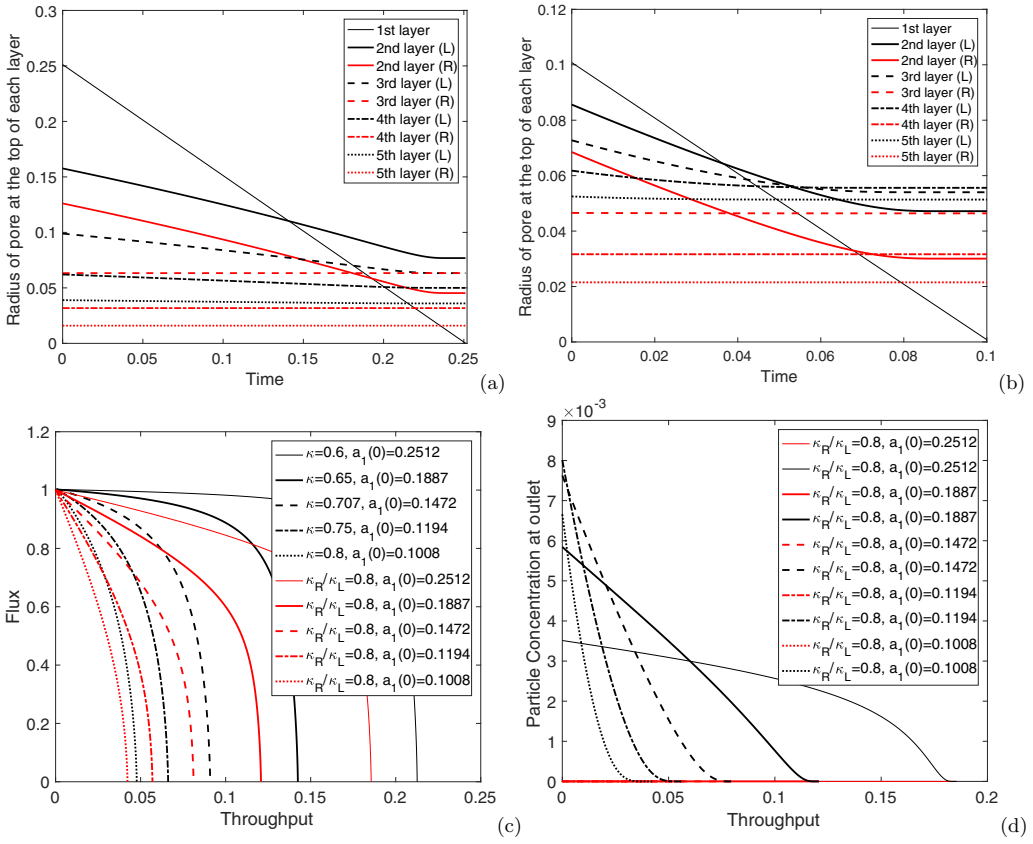

FIG. 7. Asymmetric branching model: results for membranes with initial dimensionless resistance $r_0 = 1$ and ratio of right and left branch geometric coefficients $\kappa_R/\kappa_L = 0.8$. (a) and (b) Inlet pore radius evolution in each layer [left L (black) and right R (red)]$a_{R/L,i}(x_i, t)$ for different values of the top layer initial pore radius $a_1(0)$: (a) $a_1(0) = 0.2512$ and (b) $a_1(0) = 0.1008$. (c) Total flux $q(t)$ vs throughput $v(t)$ for $a_1(0) = 0.2512, 0.1887, 0.1472, 0.1194, 0.1008$ (red curves) and also for the corresponding symmetric cases of Fig. 3 (black curves). (d) Particle concentration at outlet $c_{mj}(1, t)$ for $j = 1, \ldots, 2^{m-1}$ versus throughput for the left (black curves) and right (red curves) subbranches, with $\lambda = 30$ and $m = 5$.

curves. As shown here, the particle concentration downstream in the narrower (right) subbranch is much less than that in the left subbranch.

To characterize further the effect of breaking symmetry on filtration performance, we plot total throughput versus the geometric coefficient ratio κ_R/κ_L in Fig. 8 for branching structures with $m = 5$ layers, again with deposition coefficient $\lambda = 30$ and total initial resistance $r_0 = 1$. The geometric coefficient ratio $\kappa_R/\kappa_L \in (0, 1]$ (with no loss of generality, $\kappa_R \leqslant \kappa_L$) characterizes the degree of asymmetry, with a value of 1 being the symmetric case and asymmetry increasing as the ratio approaches zero. For each of the graphs in Fig. 8, we fixed the first layer initial pore radius (as presented in the legend) and then varied the value of κ_R/κ_L while keeping initial total resistance fixed at $r_0 = 1$. The results confirm the hypothesis suggested by the previous simulations: As the degree of asymmetry increases, filtration efficiency (as measured by total throughput over the filter lifetime) decreases. This effect is more prominent for those branching structures with larger pores in the top layer. Breaking the symmetry for those structures with smaller pores on top does not affect the performance significantly. Note that since the initial radius of the top pore a_{1_0} is held fixed as the asymmetry increases in Fig. 8, the observed variation in throughput must be due to other

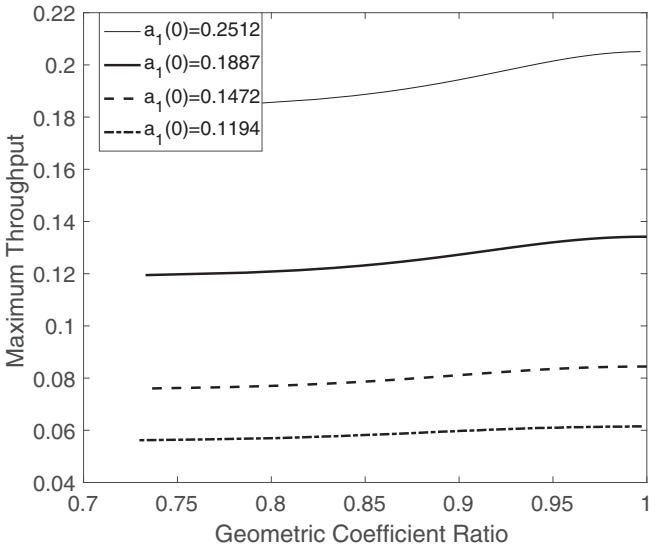

FIG. 8. Asymmetric branching model: total throughput $v(t)$ versus geometric coefficient ratio κ_R/κ_L, for several branching structures with different initial top pore radii $a_1(0)$, but the same initial resistance $r_0 = 1$. In all cases $\lambda = 30$ and $m = 5$.

effects (but note that the throughput variation seen here is much smaller than in Fig. 7, indicating that a_{1_0} has the dominant effect).

V. CONCLUSION

We have presented a simple model to quantify the effects of a bifurcating-pore membrane morphology on separation efficiency and fouling of a membrane filter. Our model accounts for Darcy flow through a simple bifurcating pore structure within the membrane and for fouling by particle adsorption within pores. Our model contains an important dimensionless parameter that must be measured for a given system: λ, the dimensionless attraction coefficient between the membrane pore wall and the particles carried by the feed solution. In principle, this parameter λ could be estimated by fitting our model results to a reliable data set, but since λ depends on properties of both membrane and feed solution, it will vary from one membrane-feed system to another and so will need to be determined for each system considered.

The focus in this paper is on development of a model that can be used to quantify the performance of a membrane filter in terms of its pore-branching characteristics. The internal morphology of real membranes is undoubtedly highly complex: Here we focus mainly on a simple symmetric layered branching pore structure characterized by two geometric coefficients: κ (which quantifies how pore size changes in the depth of the membrane) and κ_{d} (which quantifies how the layer thickness changes). In general, we compare performance of membrane filters with equal initial total membrane resistance r_0 (once the values of κ, κ_{d}, r_0, and the number of layers m are fixed for a symmetric bifurcating pore structure, the membrane structure is determined). We briefly consider the effect of introducing a restricted type of asymmetry in Secs. III B and IV B, where the same basic layered branching structure is assumed but the pores in the second layer are nonidentical, and in subsequent layers the whole structure divides into two subbranches, left and right, with pores decreasing geometrically in the depth of membrane in each subbranch. All simulations presented in this paper are for the case of flow perpendicular to the membrane surface, driven by a constant pressure drop. Although the simulations presented in the main body of the paper are for the partial differential equation-based model presented in Sec. III, in Appendix B we outline a simplified

discrete model, which provides approximate quasianalytical solutions for averaged pore radii and particle concentrations within layers and which can be useful to provide a quick guide as to the most useful regimes to explore. This discrete model was tested and found to provide reasonable approximations for systems with $m > 5$ layers, with the accuracy of predictions increasing with the number of layers.

The results of Fig. 3 for the symmetric branching case with equal-thickness layers ($\kappa_d = 1$) indicate that variations in branching structure lead to different fouling patterns within the membrane depending on the value of the geometric coefficient κ. Importantly, though the initial resistance of all membranes simulated in this figure is the same, if the value of the pore-radius geometric coefficient κ is small (meaning, with the fixed resistance constraint, that the initial pore radius at the top of membrane is large and the membrane has significant negative porosity gradients in its depth), the membrane exhibits markedly better filtration performance, as quantified by the total amount of filtrate processed under the same operating conditions (as seen earlier in [16,25]), while simultaneously offering improved particle retention. Figure 3(d) also demonstrates the important point that, for microstructured membranes, one cannot safely use the initial particle retention as a predictor of particle retention over the membrane lifetime: Particle retention may deteriorate over time.

Another important prediction of our model, borne out by Fig. 4(b), is that a membrane with more layers exhibits greater total throughput over its lifetime for the same initial resistance. This conclusion holds independently of the value of the geometric coefficient ratio, indicating that superior performance can be obtained by using microstructured membranes with small values of the geometric coefficient ratio and a large number of layers. Figure 5(b) further emphasizes the potential importance of porosity gradients, particularly in cases where the value of the dimensionless attraction coefficient λ may be small. For $\lambda = 7.5$ a branched-pore filter with initial dimensionless membrane resistance $r_0 = 1$, number of layers $m = 5$, and porosity gradients ($\kappa \approx 0.42$) can remove 99% of particles, while one that is uniformly porous removes less than 90% of particles [see orange curves in Fig. 5(b)]. At larger values of λ particle retention is much less sensitive to the value of κ. (Such considerations also reveal the importance of accurately estimating the value of the attraction coefficient λ for the system.)

In addition to the conclusions discussed above, Fig. 6 illustrates the important role that varying the layer thickness can play. This figure shows that, for all scenarios considered, optimal performance is achieved with a value of κ_d in the range (1.15,1.45), indicating that as the pores shrink in the membrane depth, the layers containing these pores should become thicker as dictated by the maximizing value of κ_d. While our simulations are not calibrated to describe a particular experimental data set, we note that for a membrane of the approximate structure considered here, it should be possible to use an experimental data set to determine the important parameter λ for a given feed solution and thence to use our results to predict the optimal structure of this type.

While in this paper we do not investigate asymmetric branching structures in detail, the results of Sec. IV B indicate the importance of such asymmetry considerations. Within the limitations of the simple asymmetry considered there, while the same general conclusions hold true regarding the favorability of negative porosity gradients in the depth of the membrane, asymmetries in the branching structure can lead to a significant drop in performance [more than 10% drop in the total throughput over the filter lifetime in some cases; see Figs. 7(c) and 8].

Though our model represents an important first step in systematically accounting for internal membrane complexity, it must be emphasized that real membranes have much more complex structure than that considered here and that in reality multiple fouling modes are operating simultaneously (our model neglects blocking of pores by particles larger than them and the caking that occurs in the late stages of filtration). Future work should address more complicated pore morphologies, scenarios with multiple fouling modes operating simultaneously, and filtration of feed solutions containing multiple particle populations.

ACKNOWLEDGMENTS

Both authors acknowledge financial support from the National Science Foundation (NSF) under Grants No. DMS-1261596 and No. DMS-1615719. P.S. was supported in part by the NSF Research Training Group in Modeling and Simulation Grant No. RTG/DMS-1646339. Several very helpful conversations with Dr. Ian Griffiths (University of Oxford) are gratefully acknowledged, as are the detailed comments provided by an anonymous reviewer.

APPENDIX A: FOULING AT THE BIFURCATIONS

The models outlined in Sec. II, for both symmetric and asymmetric branching configurations, both neglect any additional fouling that may occur at the junctions where pores bifurcate. Since it is known that in analogous physiological systems such as the cardiovascular system such junctions may be prone to deposition and formation of arterial plaques,[4] we here briefly consider how to model the effect that fouling at the junctions might have on overall system performance.

The details of the flow at a T-junction-type bifurcation will be complicated; but broadly speaking, for the model geometry we consider here, a well-developed Poiseuille flow upstream impacts a wall at the junction, where it transitions to a stagnation-point flow. The flow separates into two streams, which will enter the two pores in the downstream layer. In the spirit of developing the simplest reasonable model that captures the key physics, we assume that the rate of deposition of particulate material at the junction is proportional to the instantaneous flux of fluid and particle concentration into the junction. As deposited material accumulates, it will create some degree of blockage and increase system resistance. We assume that this additional resistance appears in series with the resistance of the pore upstream. For the symmetric branching model this translates to

$$R_i = \int_{X_{i-1}}^{X_i} \frac{8}{\pi A_i^4} dX + B \int_0^T C_i(T') Q_i(T') dT', \quad 1 \leqslant i \leqslant m-1, \tag{A1}$$

replacing the expression in (6), where $B > 0$ is a constant and $Q_i = \pi A_i^2 \bar{U}_{\mathrm{p},i}$ is the flux through each pore in the ith layer. The resistance of the pores in the mth layer remains unchanged from the previous model: $R_m = \int_{X_{m-1}}^{X_m} 8/\pi A_m^4 dX$.

For the asymmetric branching model the analogous expression for the resistance of the jth pore in layer i is

$$R_{ij} = \int_{X_{i-1}}^{X_i} \frac{8}{\pi A_{ij}^4} dX + B \int_0^T C_{ij}(T') Q_{ij}(T') dT', \quad 1 \leqslant i \leqslant m-1,\ 1 \leqslant j \leqslant 2^{i-1}, \tag{A2}$$

where $Q_{ij} = \pi A_{ij}^2 \bar{U}_{\mathrm{p},ij}$ is the flux through the jth pore in the ith layer. Again, the resistance of the pores in the mth layer and the remainder of the model are as in Sec. II B.

This modified fouling model should be solved alongside an analogously modified particle concentration equation that accounts for this additional mechanism of particle removal. Preliminary simulations however suggest that the effect of such junction fouling is negligible; hence we omit it from our presented results.

APPENDIX B: SIMPLIFIED DISCRETE MODEL

In a membrane with many layers, the system in Sec. II can be time consuming to solve numerically. However, in such situations we anticipate that the length of pores between successive bifurcations is short relative to the typical length scale of gradients in C [estimated from (8)],

[4] In the case of arterial plaque formation, however, the chief complication arises when the plaques break off from the wall and cause blockage further downstream; we do not consider such effects here.

corresponding to an assumption that $32\Lambda\mu D^2/\pi P_0 W^3 \ll 1$. For situations where a fast approximate solution is required, we thus propose a simplified model, based on (8), in which we take C_i to represent the approximate particle concentration at the downstream end of pores in layer i. Using A_i (independent of X) to then represent the average pore radius within layer i, the resistance of an individual pore in layer i [see (6)] simplifies to $R_i = 8D_i/\pi A_i^4$. A simple finite-difference approximation of (8) then gives

$$\bar{U}_{\mathrm{p},i}\frac{C_i - C_{i-1}}{D_i} = -\Lambda\frac{C_i}{A_i}, \quad 1 \leqslant i \leqslant m, \tag{B1}$$

where the averaged axial velocity within each pore in layer i, $\bar{U}_{\mathrm{p},i}$, is given by (5)–(3) as

$$\bar{U}_{\mathrm{p},i} = \frac{P_0}{\pi\mu\nu_i A_i^2 R}, \quad 1 \leqslant i \leqslant m. \tag{B2}$$

This allows the particle concentration C_i to be expressed in terms of C_{i-1} as

$$C_i = \frac{\bar{U}_{\mathrm{p},i} C_{i-1}}{\bar{U}_{\mathrm{p},i} + \Lambda D_i/A_i}, \quad 1 \leqslant i \leqslant m. \tag{B3}$$

In addition, we approximate (10) by

$$\frac{\partial A_i}{\partial T} = -\Lambda\alpha C_{i-1}, \quad 1 \leqslant i \leqslant m,$$

which means that the pore radius in the layer i shrinks proportionally to the particle concentration at the pore inlet upstream. (This is necessary since pore closure is dominated by the upstream particle concentration.) This simple model has been tested and found to provide reasonable agreement with the full partial differential equation model presented here, over a range of model parameters.

[1] E. Iritani, A review on modeling of pore-blocking behaviors of membranes during pressurized membrane filtration, Drying Tech. **31**, 146 (2013).

[2] G. Bolton, D. LaCasse, and R. Kuriyel, Combined models of membrane fouling: Development and application to microfiltration and ultrafiltration of biological fluids, J. Membrane Sci. **277**, 75 (2006).

[3] G. R. Bolton, A. W. Boesch, and M. J. Lazzara, The effect of flow rate on membrane capacity: Development and application of adsorptive membrane fouling models, J. Membrane Sci. **279**, 625 (2006).

[4] C.-C. Ho and A. L. Zydney, Effect of membrane morphology on the initial rate of protein fouling during microfiltration, J. Membrane Sci. **155**, 261 (1999).

[5] C.-C. Ho and A. L. Zydney, A combined pore blockage and cake filtration model for protein fouling during microfiltration, J. Colloid Interface Sci. **232**, 389 (2000).

[6] S. Roy, Innovative use of membrane technology in mitigation of GHG emission and energy generation, Proc. Environ. Sci. **35**, 474 (2016).

[7] R. C. Daniel, J. M. Billing, R. L. Russell, R. W. Shimskey, H. D. Smith, and R. A. Peterson, Integrated pore blockage-cake filtration model for crossflow filtration, Chem. Eng. Res. Des. **89**, 1094 (2011).

[8] A. I. Brown, P. Levison, N. J. Titchener-Hooker, and G. J. Lye, Membrane pleating effects in 0.2 μm rated microfiltration cartridges, J. Membrane Sci. **341**, 76 (2009).

[9] S. E. Skilhagen, J. E. Dugstad, and R. J. Aaberg, Osmotic power–power production based on the osmotic pressure difference between waters with varying salt gradients, Desalination **220**, 476 (2008).

[10] R. G. M. Van der Sman, H. M. Vollebregt, A. Mepschen, and T. R. Noordman, Review of hypotheses for fouling during beer clarification using membranes, J. Membrane Sci. **396**, 22 (2012).

[11] S. Giglia and G. Straeffer, Combined mechanism fouling model and method for optimization of series microfiltration performance, J. Membrane Sci. **417-418**, 144 (2012).

[12] F. Meng, S.-R. Chae, A. Drews, M. Kraume, H. S. Shin, and F. Yang, Recent advances in membrane bioreactors (MBRs): Membrane fouling and membrane material, Water Res. **43**, 1489 (2009).
[13] P. Apel, Track etching technique in membrane technology, Radiat. Meas. **34**, 559 (2001).
[14] M. P. Dalwadi, I. M. Griffiths, and M. Bruna, Understanding how porosity gradients can make a better filter using homogenization theory, Proc. R. Soc. A **471**, 20150464 (2015).
[15] I. M. Griffiths, A. Kumar, and P. S. Stewart, A combined network model for membrane fouling, J. Colloid Interface Sci. **432**, 10 (2014).
[16] I. M. Griffiths, A. Kumar, and P. S. Stewart, Designing asymmetric multilayered membrane filters with improved performance, J. Membrane Sci. **511**, 108 (2016).
[17] K. J. Hwang, C. Y. Liao, and K. L. Tung, Analysis of particle fouling during microfiltration by use of blocking models, J. Membrane Sci. **287**, 287 (2007).
[18] N. B. Jackson, M. Bakhshayeshi, A. L. Zydney, A. Mehta, R. van Reis, and R. Kuriyel, Internal virus polarization model for virus retention by the Ultipor VF grade DV20 membrane, Biotechnol. Prog. **30**, 856 (2014).
[19] D. M. Kanani, W. H. Fissell, S. Roy, A. Dubnisheva, A. Fleischman, and A. L. Zydney, Permeability-selectivity analysis for ultrafiltration: Effect of pore geometry, J. Membrane Sci. **349**, 405 (2010).
[20] A. Mehta and A. L. Zydney, Permeability and selectivity analysis for ultrafiltration membranes, J. Membrane Sci. **249**, 245 (2005).
[21] A. Mehta and A. L. Zydney, Effect of membrane charge on flow and protein transport during ultrafiltration, Biotechnol. Prog. **22**, 484 (2006).
[22] S. Mochizuki and A. L. Zydney, Theoretical analysis of pore size distribution effects on membrane transport, J. Membrane Sci. **82**, 211 (1993).
[23] Y. S. Polyakov and A. L. Zydney, Ultrafiltration membrane performance: Effects of pore blockage/constriction, J. Membrane Sci. **434**, 106 (2013).
[24] N. S. Pujar and A. L. Zydney, Charge regulation and electrostatic interactions for a spherical particle in a cylindrical pore, J. Colloid Interface Sci. **192**, 338 (1997).
[25] P. Sanaei and L. J. Cummings, Flow and fouling in membrane filters: Effects of membrane morphology, J. Fluid Mech. **818**, 744 (2017).
[26] L. J. Zeman and A. L. Zydney, *Microfiltration and Ultrafiltration: Principles and Applications* (Dekker, New York, 1996).
[27] A. L. Zydney, High performance ultrafiltration membranes: Pore geometry and charge effects, Membr. Sci. Technol. Ser. **14**, 333 (2011).
[28] U. Beuscher, Modeling sieving filtration using multiple layers of parallel pores, Chem. Eng. Technol. **33**, 1377 (2010).